Emission characteristics of water in the Universe

Poelman, Dieter Roel

Chapter 3

The excitation of water in the S140 region

Water is a key ingredient in many interstellar environments, like photon dominated regions and star forming clouds. It plays an important role in the oxygen chemistry and can act as a coolant in dense interstellar clouds and shocks. Observations and modeling of water lines thus provide powerful diagnostics of the physical conditions in interstellar emission zones. In this chapter, we consider the excitation of water in the photon dominated region S140 and its embedded sources. Homogeneous and inhomogeneous models are used to compute the differences between H_2O line transitions and profiles across the S140 region. We apply our models to previous SWAS and ISO observations of water vapour in order to make models to plan for, and to interpret, HIFI data. It is found that the low-lying transitions, e.g., 1_{10}-1_{01} and 2_{12}-1_{01}, trace the photon dominated region, whereas the high excitation lines, e.g., 3_{21}-2_{21}, 3_{03}-2_{12}, 2_{12}-1_{01} and 2_{20}-1_{11}, probe the embedded sources. Therefore, water emission in a source like S140 requires a combination of a pure photon dominated region and an embedded source in order to match the observations. Because of its good angular resolution, HIFI will be able to distinguish between a dense star forming region or a more diffuse gas component. It is therefore important for future observing programs to consider both in their predictions of the emission characteristics of water in these environments.

Based on Poelman, D. R., & Spaans, M. 2005, A&A, 440, 559-567
and Poelman, D. R., & Spaans, M. 2006, A&A, 453, 615-620

3.1 Introduction

The study of water is of great interest, not only because H_2O possesses a very large number of strong far-infrared (FIR) transitions, but also because it plays a crucial role in the chemistry of molecular clouds (Bergin et al. 1998) and can act as an important coolant in dense clouds (Neufeld et al. 1995), shocks (Draine et al. 1983; Neufeld & Melnick 1987) and circumstellar outflows (Chen & Neufeld 1995). Because of its high abundance and easy excitation in warm interstellar and circumstellar environments, water is a powerful tool to probe astrophysical conditions in a broad variety of sources, from molecular clouds to protostars.

Nonetheless, the large attenuation by terrestrial H_2O molecules has made ground-based observations nearly impossible. Therefore, observations from space-born facilities are needed (e.g., Neufeld et al. 1999; Truong-Bach et al. 1999; Wright et al. 2000). The launch of the *Infrared Space Observatory* (ISO) has made it possible to look for emission and absorption lines in warm (~ 100 K) molecular gas near young stellar objects (van Dishoeck et al. 1999), while the *Submillimeter Wave Astronomy Satellite* (SWAS) has probed H_2O and O_2 residing in cold molecular clouds (Melnick et al. 2000), as has Odin (Hjalmarson et al. 2003). The future launch of Herschel, with on board the *Heterodyne Instrument for the Far Infrared* (HIFI), will provide even better information on the physical and chemical conditions in molecular clouds by means of observing many water lines with higher angular resolution (between $13'' - 39''$, depending on frequency) and sensitivity. As more infrared and submillimeter surveys are planned in the future (e.g., SOFIA, JWST), more models to interpret the data from these instruments are needed.

One way to retrieve information from an observed object is through the emission properties on one hand and through understanding the spectrum on the other hand. Together, a complete picture arises of the region. Line profiles of molecules contain important information on the conditions of the regions they occupy, such as the density, and the velocity structure. Retrieving information from these lines requires accurate modeling. However, the interpretation of the line shapes has to be treated with great caution. Rawlings & Yates (2001) noted that the classic signature of infall (an asymmetric double-peaked line which possesses a blue wing that is stronger than the red wing) could dissapear when molecules are depleted in spite of infall velocity fields. Moreover, Lee et al. (2004) argued that line observations can be misunderstood if one does not consider the variations in abundance with time or with radius.

In this chapter we discuss the excitation of water in photon dominated regions (PDRs). As a test case we take the S140 region because it has been probed extensively in the past with SWAS and will be examined in the future with HIFI, as part of key programs. The results presented herein

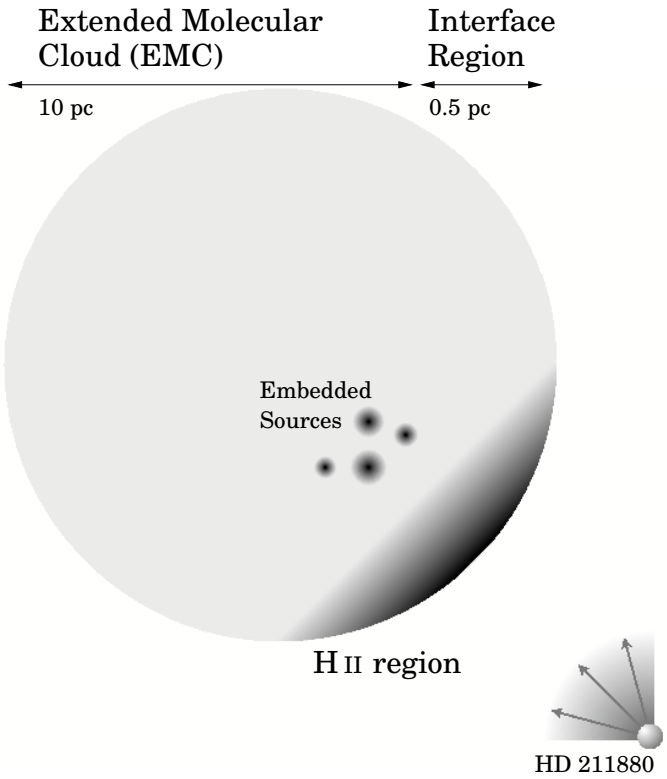

Figure 3.1: Schematic impression of the S140 interface region and extended molecular cloud.

are obtained with the β3D code, described in Chapter 2, combined with the inhomogeneous numerical code of Spaans (1996) and Spaans & van Dishoeck (1997). Section 3.2 describes briefly the S140 region. Sections 3.3 and 3.4 are used to interpret the results from 3D-(in)homogeneous models. In Section 3.5, line profiles are shown throughout the S140 region. We summarize and discuss the results in Sect. 3.6.

3.2 The molecular cloud S140

The molecular cloud lies at a distance of ~ 900 pc (Crampton & Fisher 1974) and is illuminated from the south-western side by the BOV star HD 211880. The star is located about ~ 7′ (1.85 pc) from the edge of the cloud and offers a source of impinging ultraviolet (UV) photons. The cloud extends over more than 30′ (8 pc) and contains a dense core in which star formation is occuring.

The molecular cloud consists of two parts: (i) the interface region near the south-west edge of the cloud (PDR), and (ii) the extended molecular cloud (EMC). Here focus is on the interface region, as this region is a far more interesting object to probe the behaviour of water with its high H_2O abundance relative to the EMC. A schematic impression of the S140 molecular cloud is shown in Fig. 3.1.

In the past, models were able to reproduce the observations of the extended emission of neither [CI] (Keene et al. 1985) and [CII] (Stutzki et al. 1988) deep into the cloud, nor the intense ^{13}CO 6-5 emission in some regions (Graf et al. 1990). This information, together with the CO maps by Falgarone & Perault (1988), led to the suggestion that interstellar clouds are very inhomogeneous in nature. In this way, the UV radiation penetrates deeper into the cloud, hence heating up a more extended region, as is suggested from observations.

Most previous models of S140 (e.g., Ashby et al. 2000) have assumed a spherically symmetric cloud with temperature and density power laws. Even though they can reproduce well the observed value of the intensity of the 557 GHz 1_{10}-1_{01} ground-state transition of ortho-$H_2^{16}O$, being acquainted with the inhomogeneous structure of molecular clouds from observations and in order to explain and predict more accurately various line transitions, we make use of density, temperature and abundance (relative to H_2) distributions as calculated with the inhomogeneous Monte Carlo code of Spaans (1996), further described in Spaans & van Dishoeck (1997). As such, the first attempt is made to model the water emission in S140 in an inhomogeneous way.

The Monte Carlo code calculates the chemical structure and thermal balance in PDRs, as well as the distribution of the water abundance and molecular hydrogen density simultaneously. A chemical network including 291 reactions between 51 species consisting of the elements hydrogen (H), carbon (^{12}C), oxygen (O), iron (Fe), magnesium (Mg), and Polycyclic Aromatic Hydrocarbons (PAHs, with charges −1, 0, +1) is used. The gas abundances for S140, are taken to be 2×10^{-4}, 5×10^{-4}, 2.5×10^{-7} and 1.3×10^{-6} for C, O, Fe and Mg, respectively. For carbon this implies that about 50% of the solar abundance is present in the gas phase, which is comparable with the values found in diffuse clouds (Cardelli et al. 1993).

Mechanisms for converting the UV flux into gas heating are (1) photoelectric emission from small dust grains and large molecules like PAHs (Bakes & Tielens 1994; Spaans et al. 1994), (2) neutral carbon ionization, (3) H_2 photodissociation, (4) far-ultraviolet (FUV) pumping followed by collisional de-excitation of vibrationally excited H_2 in a two level approximation, and (5) H_2 formation from FUV-produced hydrogen atoms on grain surfaces. In addition, (6) cosmic-ray heating may also contribute to the heating deep into the cloud, and (7) OI may heat the gas through the collisional de-excitation of the $^3P_1$ fine structure level excited by (dust) conti-

nuum radiation.

For the cooling, the infrared fine-structure lines from atoms C, C^+, O, Si, and Fe have been taken into account. The lowest 20 rotational levels of CO are calculated in statistical equilibrium and their contribution to the cooling is included. H_2 rotational cooling is considered, as well as cooling due to water through an adopted cooling function (Neufeld & Melnick 1987). The contribution of water to the total cooling rate amounts to $10-20\%$ around the clump density of 10^5 cm^{-3} and for temperatures of $40-60$ K. The CO molecule dominates the cooling for these conditions.

The computed temperature, density and water abundance distribution is then used as input for the β3D line transfer code. This approach leads to a more accurate treatment of the complex chemical and thermal structure of the PDR, than when a temperature and H_2O abundance are simply imposed.

3.3 Models

This section consists of three parts. The first part describes the results from the homogeneous PDR model, the second part describes the outcome of the inhomogeneous models. The third part is attributed to the excitation characteristics of water in an embedded source, known to be present in the PDR (Harvey et al. 1978; Preibisch et al. 2001, 2002).

3.3.1 Homogeneous PDR model

The incident radiation field, taken to be $I_{\rm UV} = 140$ with respect to the Draine (1978) field, is consistent with the enhancement at the edge of the cloud near the BOV star HD 211880. An isotropic component, $I_{\rm UV} = 1$, of the average interstellar radiation field has also been taken into account. We adopt a generic mean total hydrogen density of $n_{\rm H} = n({\rm H}) + 2n({\rm H_2}) = 2 \times 10^4$ cm^{-3} over a region 0.5 pc in extent, corresponding to a visual extinction $A_{\rm V}$ of ≈ 20 mag, in agreement within a factor of $\sim 1.5-2$ with observations (Hayashi et al. 1985; Zhou et al. 1994). For areas where H_2O is present, hydrogen is totally molecular (the main part of the UV radiation is already absorbed), and therefore $n_{\rm H} = 2n({\rm H_2})$. The model is run on a 81^3 grid, corresponding to a resolution of 0.006 pc.

The temperature distribution for the gas and dust is shown in Fig. 3.2. The gas (dust) temperature is ~ 150 K (40 K) at the western edge of the cloud, and drops to about 30 K (30 K) deeper inside the cloud. The dust temperature stays far below the gas temperature at the west side, but becomes slightly larger or equal to the gas temperature towards the opposite edge. It is worth noting that dust plays an important role in the excitation of water. It absorbs the interstellar FUV and visible radiation field

Table 3.1: Homogeneous model

λ_{ul} [μm]	Transition	E_{ul} [K]	X_{ul} [s]	Average* intensity [erg cm^{-2} s^{-1} sr^{-1}]	Peak intensity [erg cm^{-2} s^{-1} sr^{-1}]	Average† around peak intensity [erg cm^{-2} s^{-1} sr^{-1}]	$n_{\rm cr}{}^{*}$ [cm^{-3}]
538.2	o-H_2O 1_{10}-1_{01}	26.7	3.458×10^{-3}	4.0×10^{-8}	1.0×10^{-7}	9.2×10^{-8}	3.5×10^{7}
179.5	o-H_2O 2_{12}-1_{01}	80.2	5.593×10^{-2}	5.6×10^{-7}	1.4×10^{-6}	1.3×10^{-7}	5.0×10^{8}
108.1	o-H_2O 2_{21}-1_{10}	133.2	2.564×10^{-1}	8.2×10^{-10}	2.0×10^{-9}	1.8×10^{-9}	3.6×10^{9}
180.5	o-H_2O 2_{21}-2_{12}	79.7	3.058×10^{-2}	5.9×10^{-11}	1.4×10^{-10}	1.3×10^{-10}	6.6×10^{8}
174.6	o-H_2O 3_{03}-2_{12}	82.4	5.048×10^{-2}	5.7×10^{-10}	1.0×10^{-9}	8.9×10^{-10}	7.7×10^{8}
260.0	o-H_2O 3_{12}-2_{21}	55.4	2.634×10^{-3}	1.8×10^{-12}	4.0×10^{-12}	3.7×10^{-12}	4.8×10^{7}
273.2	o-H_2O 3_{12}-3_{03}	52.7	1.648×10^{-2}	1.1×10^{-11}	2.4×10^{-11}	2.2×10^{-11}	2.8×10^{8}
269.3	p-H_2O 1_{11}-0_{00}	53.5	1.842×10^{-2}	1.7×10^{-7}	4.9×10^{-7}	4.5×10^{-7}	1.6×10^{8}
303.4	p-H_2O 2_{02}-1_{11}	47.5	5.835×10^{-2}	1.7×10^{-9}	4.4×10^{-9}	4.1×10^{-9}	8.9×10^{7}
101.0	p-H_2O 2_{20}-1_{11}	142.6	2.607×10^{-1}	1.9×10^{-10}	5.4×10^{-10}	5.0×10^{-10}	3.8×10^{9}
398.6	p-H_2O 2_{11}-2_{02}	36.1	7.062×10^{-3}	3.3×10^{-11}	6.4×10^{-11}	5.6×10^{-11}	8.7×10^{7}

Notes – * Average intensity over the whole cloud.

† Intensity averaged over the HIFI FWHM beam size (*http://www.sron.rug.nl/hifiscience/*) for a beam centered on the peak emission.

* Critical density evaluated at 100 K.

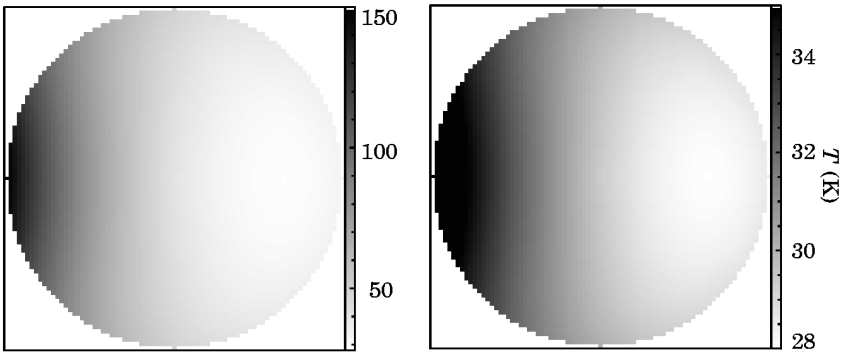

Figure 3.2: Gas (*left*) and dust (*right*) temperatures (K) when taking a vertical slice through the centre of the sphere for the homogeneous model. The star HD 21880 is located at the left of both images.

and emits the absorbed energy in the far infrared, offering a source of excitation for water. However, as the dust temperature is rather moderate throughout the PDR, its influence is limited. Computed water abundances vary from $\sim 10^{-10}$ to $\sim 10^{-6}$, relative to the hydrogen density $n_{\rm H}$, with an average abundance of 1.4×10^{-7}. At the western side of the cloud, where the star is located, the abundance reaches its minimum value due to photodissociation of water by the FUV radiation field (Section 1.2). Deeper into the cloud, the radiation field is attenuated by dust, resulting in a higher abundance. In calculating the water abundance at temperatures appropriate to interstellar clouds, a value of 0.3 is chosen for the branching ratio leading to H_2O in the dissociative recombination of H_3O^+ with a rate coefficient of $3.3 \times 10^{-7}\,(T/300)^{-0.3}$ cm^3 s^{-1} (see Section 1.2). This branching ratio is higher than the value of 0.05 suggested by Williams et al. (1996), but is consistent with the results of Vejby-Christensen et al. (1997).

Average and peak intensities, as well as intensities averaged over the HIFI FWHM beam size at the transition frequency of the particular line for a beam centered on the peak emission are listed in Table 3.1. Figure 3.3 shows maps of the predicted distribution of the intensities for various transitions for ortho- and para-H_2O as we would see them on the sky, convolved with a beam size of $0.3''$, i.e., $\sim$the angular extent that corresponds to one gridpoint.

To interpret the results, the distribution of the gas and dust temperature, the abundance of water in the cloud, the density of the medium, as

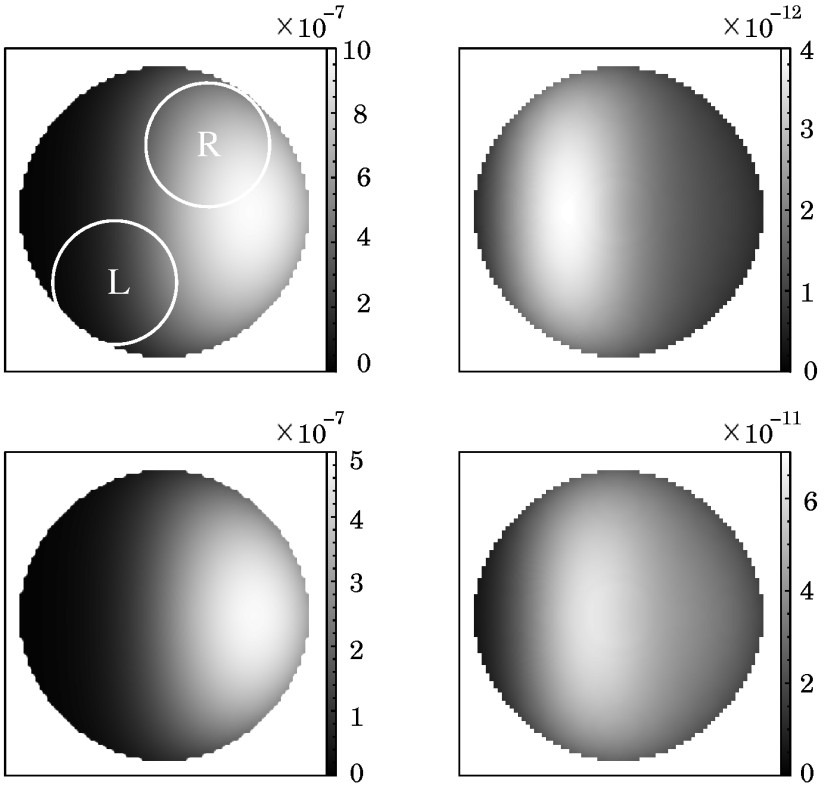

Figure 3.3: Distribution of the intensities [erg cm^{-2} s^{-1} sr^{-1}] for various transitions of ortho-(*top*) and para-(*bottom*) H_2O. The top left and right panel depicts the 1_{10}-1_{01} and 3_{12}-2_{21} transition, respectively. Bottom left and right panel plots the 1_{11}-0_{00} and 2_{11}-2_{02} lines. The star HD 211880 is located to the left of the figures. The two circles L and R in the upper left plot represent the HIFI beam when zooming in at two different positions in the PDR (see Section 3.5).

well as optical depth effects need to be taken into account. Since the overall mean density of hydrogen is 2×10^4 cm^{-3}, far below the critical density for all the transitions (of the order of 10^8 cm^{-3} or higher), the lines are subthermally excited. This means that collisional de-excitation is less important than spontaneous emission, which results in a distribution of the level populations deviating from local thermodynamic equilibrium (LTE, Section 1.3).

In general, the emission will originate from a surface layer with a thick-

ness corresponding to an optical depth $\tau_{ij} \sim 1$. The position where $\tau_{ij} \sim 1$ varies for every transition. Optically thick lines can be used to probe the physical conditions in the outer ($\tau_{ij} \lesssim 1$) layers of the cloud. Lines which are optically thin can be used to probe the physical conditions throughout the cloud. A peak in intensity for a certain transition will occur at places where the temperature is high enough to excite the line and will depend on the column of H_2O along the line of sight. The o-H_2O 1_{10}-1_{01} transition peaks near the east edge of the cloud where the temperature of the gas drops to ~ 60 K, the perfect regime to excite the line. Transitions with a higher upper energy level, e.g., o-H_2O 3_{12}-2_{21} , have their peak shifted towards the edge where the impinging radiation heats up the gas. Note that HIFI with its high angular resolution will be able to see this shift. Depending on the frequency of the transition, the beam will be ~ 5 times smaller than the PDR.

We find that the o-H_2O 2_{12}-1_{01} transition is the strongest, with an average intensity of $\sim 5 \times 10^{-7}$ erg cm^{-2} s^{-1} sr^{-1}. Other transitions are weaker by a factor of 5 and higher.

3.3.2 Inhomogeneous PDR and EMC models

The inhomogeneous nature of molecular clouds is well established from observations of extended [CI] and [CII] emission (e.g., Keene et al. 1985; Plume et al. 1994) and has been modeled by various groups (e.g., Meixner & Tielens 1993; Spaans 1996; Stoerzer et al. 1996). It is therefore natural to explore the excitation of H_2O in models incorporating high density clumps embedded in a low density interclump medium. In analogy with the homogeneous model, the inhomogeneous models are run on a 81^3 grid.

In this section we not only cover the excitation of water in the PDR but also in the EMC core, in order to fully interpret the results. We define the molecular cloud core as that part of the EMC that encloses the PDR and lies in one SWAS beam. What is left outside the molecular cloud core is denoted as the EMC.

The clumpy models have three free parameters: (i) the volume filling factor F, which gives the fraction of the total volume that is occupied by the clumps, (ii) a clump size l_c, which fixes the extinction through an individual clump, and (iii) the clump-interclump density ratio R_{ic}. For the PDR a fixed incident radiation field has been taken $I_{UV} = 140$ with respect to the Draine (1978) field, as well as a mean total hydrogen density $\langle n_H \rangle = 2 \times 10^4$ cm^{-3}, as in the case of the homogeneous model. The mean total hydrogen density obeys $\langle n_H \rangle = F n_c + (1-F) n_{ic}$. Here n_c and n_{ic} indicate the clump and interclump density, respectively. For the EMC core, the enhancement factor decreases to $I_{UV} \approx 30-50$ because of geometric dilution, and a mean total hydrogen density $\langle n_H \rangle$ of 10^3 cm^{-3} is adopted over a region 10 pc in extent. The average hydrogen density of the EMC is not well constrained by obser-

Table 3.2: Inhomogeneous model parameters

Model	size [pc]	n_c [cm^{-3}]	n_{ic} [cm^{-3}]	F [%]	R_{ic}	l_c [pc]	$X(H_2O)$	Δv_d [km s^{-1}]
PDR I	0.5	4×10^5	1×10^4	2.5	40	0.03	1×10^{-8}	1.2
PDR II	0.5	2×10^5	1×10^4	5	20	0.03	2×10^{-8}	1.2
PDR III	0.5	6×10^4	6×10^3	20	10	0.03	2×10^{-8}	1.2
EMC	10	3000	300	25	10	0.6	7×10^{-10}	0.7

vations, but the adopted value approximates those derived from the total ^{13}CO column density divided by the size of the cloud (Blair et al. 1978; Plume et al. 1994).

Table 3.2 gives the parameters used for the different models. Three models are run for the PDR and one for the EMC core. The PDR clump densities range from 3×10^4 cm^{-3} to 2×10^5 cm^{-3}, whereas interclump densities vary between 3×10^3 cm^{-3} and 5×10^3 cm^{-3}. Different volume filling factors were incorporated, ranging from 2.5% to 20%. In the PDR models, the clump size has been taken constant, being 0.03 pc in diameter. The clump size in the EMC core is taken to be 20 times larger than the clump size in the PDR, equal in proportion to the ratio in scale size. The velocity dispersion is taken to be 1.2 km s^{-1} in the PDR (Zhou et al. 1994), and 0.7 km s^{-1} in the EMC core, assuming a weaker turbulent velocity component in comparison with the v_{turb} of the PDR. The larger PDR velocity width simply reflects our assumption that the embedded sources, being present in the PDR and not in the EMC, inject some additional turbulent motions (IRS1–3, Blair et al. 1978; Beichman et al. 1979; Evans et al. 1989). This seems reasonable given that star-forming molecular cores tend to have larger (non-thermal) velocity widths than quiescent cores. The clumps are distributed randomly in the interclump medium, and clump and interclump gas join smoothly with a density gradient.

Due to the clumpiness, radiation transport will differ from that in the homogeneous model. The UV radiation penetrates deeper into a clumpy region than into a cloud in which the gas is homogeneously distributed, leading to a lower water abundance because of enhanced photodissociation (Spaans & van Dishoeck 2001). The average water abundance in comparison with the homogeneous model drops by a factor of ~ 10. Note that these clumps are low-temperature water reservoirs. Inhomogeneity also affects the temperature structure, resulting in enhanced temperatures deeper into the interclump medium of the cloud. However, temperatures inside the clumps drop due to enhanced shielding. The result is an increase in the volume averaged gas temperature (~ 78 K for PDR I), compared to the homogeneous PDR model (~ 52 K). However, the mass-weighted average gas

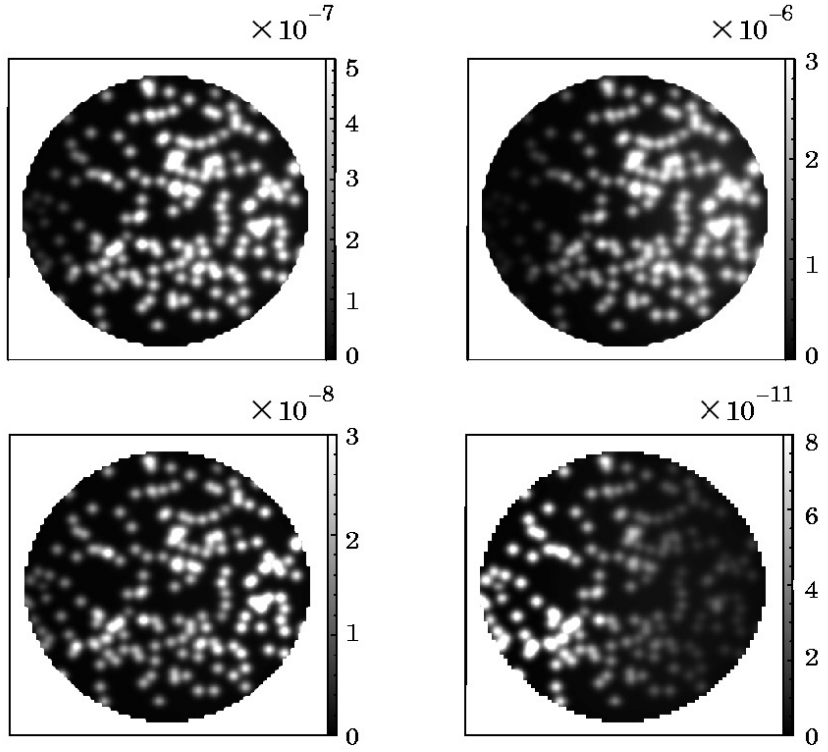

Figure 3.4: Distribution of the intensities [erg cm^{-2} s^{-1} sr^{-1}] for various transitions of ortho-H_2O using the PDR I model. The top left and right panels depict the 1_{10}-1_{01} and 2_{12}-1_{01} transitions. Bottom left and right panels plot the 2_{21}-1_{10} and 3_{12}-2_{21} line. The star HD 211880 is located to the left of the figures.

temperatures in the inhomogeneous models are 88 K, 70 K and 46 K for PDR I, PDR II and PDR III, respectively, and 52 K for the homogeneous model. This means that most of the mass of the cloud is located in cold clumps.

Average and peak intensities of various transitions for the PDR are shown in Table 3.3, and for the molecular cloud core, i.e., that part of the EMC lying at the southwest of the cloud which encloses the PDR in Table 3.4. Fig. 3.4 and 3.5 show maps of the predicted distribution of the intensities for various transitions.

The intensity of the o-H_2O 1_{10}-1_{01} line in the homogeneous PDR model is a factor of a few lower than in PDR I and PDR II, and equals that of PDR III. The strongest transition we find is the 2_{12}-1_{01}, in all the models.

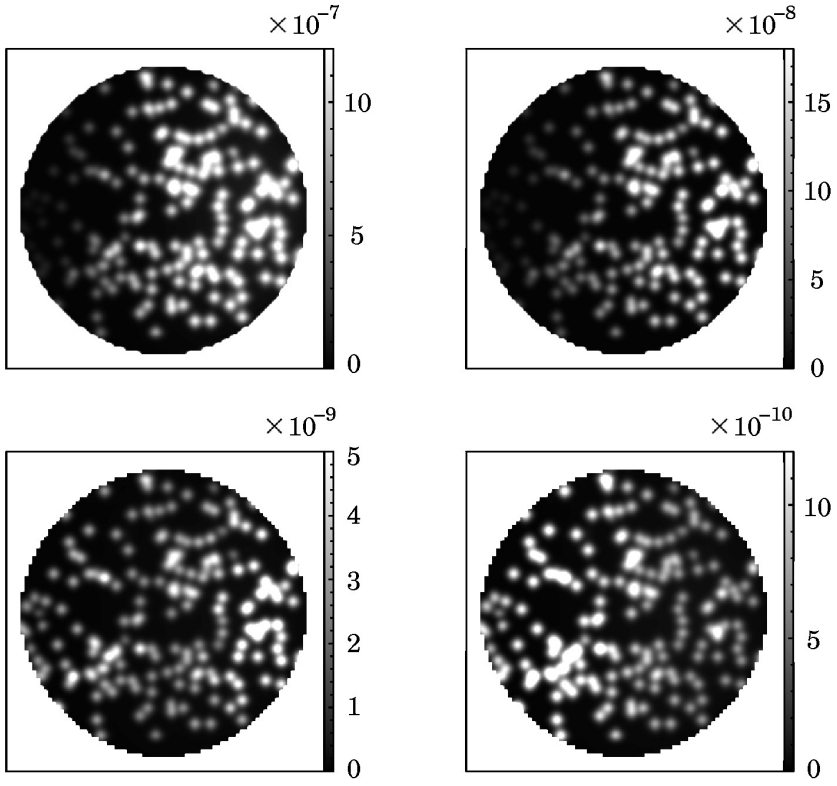

Figure 3.5: Distribution of the intensities [erg cm^{-2} s^{-1} sr^{-1}] for various transitions of para-H_2O using the PDR I model. The top left and right panels depict the 1_{11}-0_{00} and 2_{02}-1_{11} transitions. Bottom left and right panels plot the 2_{20}-1_{11} and 2_{11}-2_{02} line. The star HD 211880 is located to the left of the figures.

Table 3.3: Intensities for the inhomogeneous PDR models

Model	Transition	Average intensity	Peak intensity	Average around peak intensity*
		[erg cm^{-2}s^{-1}sr^{-1}]	[erg cm^{-2}s^{-1}sr^{-1}]	[erg cm^{-2}s^{-1}sr^{-1}]
PDR I	o-H_2O 1_{10}-1_{01}	1.1×10^{-7}	1.9×10^{-6}	2.2×10^{-7}
	o-H_2O 2_{12}-1_{01}	6.2×10^{-7}	6.6×10^{-6}	1.4×10^{-6}
	o-H_2O 2_{21}-1_{10}	5.7×10^{-9}	1.7×10^{-7}	9.1×10^{-9}
	o-H_2O 2_{21}-2_{12}	4.1×10^{-10}	1.2×10^{-8}	6.5×10^{-10}
	o-H_2O 3_{03}-2_{12}	4.7×10^{-9}	1.2×10^{-7}	8.0×10^{-9}
	o-H_2O 3_{12}-2_{21}	1.3×10^{-11}	5.4×10^{-10}	2.8×10^{-11}
	o-H_2O 3_{12}-3_{03}	7.8×10^{-11}	3.2×10^{-9}	1.7×10^{-10}
	p-H_2O 1_{11}-0_{00}	2.5×10^{-7}	3.7×10^{-6}	7.2×10^{-7}
	p-H_2O 2_{02}-1_{11}	2.7×10^{-8}	8.1×10^{-7}	5.8×10^{-8}
	p-H_2O 2_{20}-1_{11}	8.8×10^{-10}	2.3×10^{-8}	1.7×10^{-9}
	p-H_2O 2_{11}-2_{02}	2.7×10^{-10}	7.8×10^{-9}	4.4×10^{-10}
PDR II	o-H_2O 1_{10}-1_{01}	7.3×10^{-8}	6.7×10^{-7}	1.5×10^{-7}
	o-H_2O 2_{12}-1_{01}	7.3×10^{-7}	5.7×10^{-6}	1.8×10^{-6}
	o-H_2O 2_{21}-1_{10}	1.8×10^{-9}	2.6×10^{-8}	3.1×10^{-9}
	o-H_2O 2_{21}-2_{12}	1.3×10^{-10}	1.9×10^{-9}	2.2×10^{-10}
	o-H_2O 3_{03}-2_{12}	1.5×10^{-9}	2.2×10^{-8}	2.6×10^{-9}
	o-H_2O 3_{12}-2_{21}	4.3×10^{-12}	7.8×10^{-9}	1.1×10^{-11}
	o-H_2O 3_{12}-3_{03}	2.5×10^{-11}	4.7×10^{-10}	6.3×10^{-11}
	p-H_2O 1_{11}-0_{00}	2.5×10^{-7}	2.5×10^{-6}	8.6×10^{-7}
	p-H_2O 2_{02}-1_{11}	7.7×10^{-9}	1.5×10^{-7}	1.7×10^{-7}
	p-H_2O 2_{20}-1_{11}	3.5×10^{-10}	5.9×10^{-9}	7.8×10^{-10}
	p-H_2O 2_{11}-2_{02}	8.4×10^{-11}	1.5×10^{-9}	1.8×10^{-10}
PDR III	o-H_2O 1_{10}-1_{01}	2.7×10^{-8}	2.2×10^{-7}	1.1×10^{-7}
	o-H_2O 2_{12}-1_{01}	3.9×10^{-7}	3.0×10^{-6}	1.6×10^{-6}
	o-H_2O 2_{21}-1_{10}	2.0×10^{-10}	1.6×10^{-9}	5.9×10^{-10}
	o-H_2O 2_{21}-2_{12}	1.4×10^{-11}	1.1×10^{-10}	4.2×10^{-11}
	o-H_2O 3_{03}-2_{12}	8.8×10^{-11}	3.8×10^{-10}	1.0×10^{-10}
	o-H_2O 3_{12}-2_{21}	2.1×10^{-13}	1.5×10^{-12}	5.3×10^{-13}
	o-H_2O 3_{12}-3_{03}	1.2×10^{-12}	9.1×10^{-12}	2.7×10^{-12}
	p-H_2O 1_{11}-0_{00}	1.5×10^{-7}	1.4×10^{-6}	6.9×10^{-7}
	p-H_2O 2_{02}-1_{11}	4.6×10^{-10}	4.0×10^{-9}	1.1×10^{-9}
	p-H_2O 2_{20}-1_{11}	6.9×10^{-11}	9.5×10^{-10}	2.8×10^{-10}
	p-H_2O 2_{11}-2_{02}	4.8×10^{-12}	2.7×10^{-11}	7.4×10^{-12}

* Intensity averaged over the HIFI FWHM beam size (*http://www.sron.rug.nl/hifiscience/*) for a beam centered on the peak emission.

This transition has an upper state energy of ~ 80 K above ground level. The gas temperatures in the models are sufficient to excite this transition. All other transitions, except for the p-H_2O 1_{11}-0_{00}, are a few orders of magni-

Table 3.4: Inhomogeneous EMC model

Model	Transition	Average intensity [erg cm^{-2}s^{-1}sr^{-1}]
EMC core	o-H_2O 1_{10}-1_{01}	1.3×10^{-11}
	o-H_2O 2_{12}-1_{01}	5.4×10^{-11}
	o-H_2O 2_{21}-1_{10}	2.7×10^{-14}
	o-H_2O 2_{21}-2_{12}	1.9×10^{-15}
	o-H_2O 3_{03}-2_{12}	2.9×10^{-14}
	o-H_2O 3_{12}-2_{21}	1.5×10^{-16}
	o-H_2O 3_{12}-3_{03}	9.1×10^{-16}
	p-H_2O 1_{11}-0_{00}	2.4×10^{-11}
	p-H_2O 2_{02}-1_{11}	6.0×10^{-14}
	p-H_2O 2_{20}-1_{11}	5.1×10^{-15}
	p-H_2O 2_{11}-2_{02}	2.2×10^{-15}

Table 3.5: Antenna temperatures of the o-H_2O 1_{10}-1_{01} transition

Model	Antenna temperature $T_A{}^*$ [K]
Homogeneous	0.08
PDR I	0.25
PDR II	0.17
PDR III	0.07
EMC core	3.6×10^{-4}
EMC	$3\times10^{-4}-3\times10^{-3}$

tude weaker than the two lowest-lying transitions. To excite these high-lying transitions, elevated temperatures are needed.

Snell et al. (2000) mapped with SWAS a larger region of S140 than only the PDR, including several positions on the molecular cloud. They find no significant 557 GHz water emission emanating from these areas (e.g., outside the molecular cloud core), in agreement with our results (Table 3.4). The contribution of the EMC core to the total signal is negligible in comparison with the PDR. This minor contribution is due to the low gas density, which results in little excitation of the H_2O molecule. Freeze-out of water is not required to explain the SWAS non-detections away from the PDR. However, the derived physical conditions indicate that freeze-out of water does occur. From Bergin et al. (1995) we find a depletion factor of about $2-3$ (see Section 3.6).

From the average intensities, antenna temperatures are derived for the 557 GHz transition as seen in Table 3.5, corrected for beam dilution. In the case of the PDR a beam dilution factor of 2 is adopted. Note that the exact beam dilution factor is uncertain. Since the antenna temperatures scale inversely in proportion to the beam dilution factor, the results presented in Table 3.5 will differ when an alternative beam dilution factor is incorporated. The total antenna temperature is the weighted sum of the PDR and EMC contributions. PDR I and PDR II in Table 3.3 yield, when combined with Table 3.4, a value consistent with the observation of SWAS, i.e., $T_{\rm A}{}^{*} \approx 0.25$ K, (Ashby et al. 2000; Snell et al. 2000) for the ground-state transition of ortho-H_2O. At face value, PDR I is in closest agreement with this observation.

From Figs. 3.4 and 3.5, it is seen that the o-H_2O 1_{10}-1_{01} ground-state transition peaks near the eastern edge of the cloud. The bulk of the emission emanates from the individual clumps. At the western side of the cloud, the water abundance drops due to dissociation, still, for higher transitions, we see that the majority of the emission is shifted towards the western edge of the cloud. The H_2O emission arises mainly from the warm, $\sim 80-110$ K, clump edges, where the gas temperature is higher than in the interiors of the clumps. On the other hand, the clump edge water abundance is a factor of ~ 10 lower compared to the insides of the clumps, but still a factor of ~ 10 higher than in the interclump medium. The 557 GHz line traces mostly the total column of water, while it is evident from Table 3.3 that the higher excitation lines differ from one model to the other more strongly.

Again, HIFI will be able to confirm the predicted shift towards the western edge of the higher water transitions because of its good angular resolution. Also, the inhomogeneity of the medium can be constrained through water line observations, provided a number of lines are detected to confirm the temperature and density simultaneously. With the spectral resolution of HIFI, line profiles will be resolved which in their turn give information on the velocity structure, i.e., kinematics of the clumps. Tracers of outer layers of photon-dominated molecular clumps, such as atomic [CI], [CII] and mid-J CO transitions, probe also varying physical conditions of the emitting regions, since their critical densities vary from each other. Together with future water line observations, a complete picture arises from these dense emission zones.

3.4 Spherical embedded source models

Before going to Sect. 3.5 in which we model line profiles for the 1_{10}-1_{01} transition in the S140 region, we calculate the radiative transfer of certain transitions of H_2O when an embedded source is incorporated into the models of the S140 PDR. As known from observations (IRS 1 to 3, Evans et

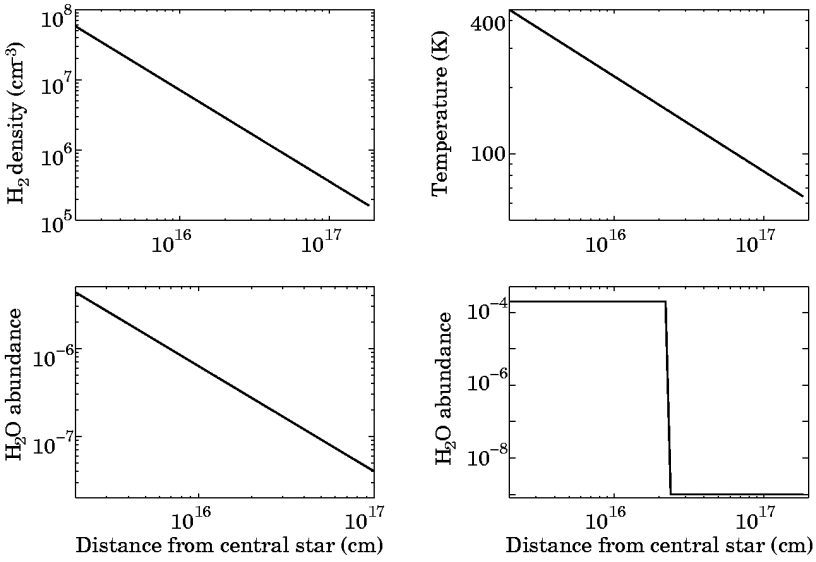

Figure 3.6: *Upper panels*: the distribution of density (*left*) and temperature (*right*) as a function of position from the embedded source. *Lower panels*: the water abundance distribution, relative to H_2, as a function of position from the embedded source for two (model I (*left*); model II (*right*)) different scenarios.

al. 1989), an embedded cluster of infrared sources is part of the S140 molecular cloud. The temperature and density structure characterizing these sources are different from the ones adopted in Section 3.3.2 for the PDR, and is therefore a useful extension of the performed calculations in Section 3.3.2.

The calculations have been performed in 1D (100 radial shells), with an adopted size of 0.06 pc and 0.12 pc for the embedded source in model I and II, respectively. Using spherical symmetry, the resulting level populations have been rotated to become a 3D solution from which the intensities have been computed. No systematic velocity field is included, but a velocity dispersion, $\Delta v_{\rm es} = (v_{\rm th}^2 + v_{\rm turb}^2)^{1/2}$, of 2 km s^{-1} is adopted. The temperature and density structures of the embedded source were derived by van der Tak et al. (2000, 2003), using a power-law density structure $n = n_0(r/r_0)^{-\alpha}$, and are plotted in Fig. 3.6. Following Boonman et al. (2003), our density increases from a few times 10^5 cm^{-3} at the edge to almost 10^8 cm^{-3} in the centre of the embedded source for both models. We assume, for simplicity, that the temperature of the gas is coupled to the dust because of the high densities, as opposed to the deviating gas and dust temperatures in the PDR and EMC. In models I and II, the temperature rises from, respectively, 80 K and 60 K

Table 3.6: Observed ISO line intensities [erg cm^{-2} s^{-1} sr^{-1}] for S140 IRS 1

Transition and wavelength			
113.5 μm	136.5 μm	174.6 μm	179.5 μm
4_{14}-3_{03}	3_{30}-3_{21}	3_{03}-2_{12}	2_{12}-1_{01}
$< 6.8 \times 10^{-6}$	$< 8.6 \times 10^{-6}$	7.1×10^{-5}	$< 4.5 \times 10^{-5}$

at the edge towards 450 K in the centre. The corresponding H_2O abundance profiles are plotted in Fig. 3.6. Note that the average H_2O abundance is a factor 20 to 2×10^3 higher, respectively, in Model I and II, in comparison to the average abundance in the PDR. The adopted water abundance profiles are merely to illustrate the effects that are expected to result when water molecules are thermally released from warm dust grains (cf. Boonman et al. 2003). Note that our embedded sources are $\sim 2 \times 10^{17}$ cm in size, compared to $\sim 10^{18}$ cm in Boonman et al. 2003. We feel that this is appropriate because 10^{17} cm is approximately the size of the adopted clumps in Section 3.3.2. Hence, beyond 10^{17} cm photo-dissociation of water dominates. Table 3.6 lists the observed ISO line intensities, as presented in Boonman et al. (2003). These line fluxes [W cm^{-2} μm^{-1}] have been converted into line intensities [erg cm^{-2}s^{-1}sr^{-1}] by adopting a beam size of $\sim 78''$ (~ 0.4 pc at the distance of S140) in order to facilitate comparison. The resulting intensities of the two adopted models are listed in Table 3.7, together with the results found in Section 3.3.2 for the PDR without embedded sources.

Higher densities and temperatures lead to stronger intensities for the high-lying transitions compared to the PDR intensities. We find that the 1_{10}-1_{01} line is a factor ~ 10 too high compared to the observed SWAS value for both the models. However, beam dilution effects are likely to alleviate this (Spaans & van Dishoeck 2001). The predicted intensity for the 3_{03}-2_{12} line at 174.6 μm is less than a factor of two lower than the observed value of 7.1×10^{-5} erg cm^{-2}s^{-1}sr^{-1} for model II, while model I is lower by a factor of ~ 3. A core of water, as in model II, is preferred to model this transition. The predicted intensities for the 2_{12}-1_{01} line at 179.5 μm and the 3_{30}-3_{21} line at 136.5 μm are in good agreement with the observed upper limits for both models. The observed upper limit for the 4_{14}-3_{03} line at 113.5 μm is best reproduced by model I. Model II produces too much intensity for this transition by a factor of ~ 20.

The intensities listed in Table 3.7 show that water emission from a PDR source, like S140, requires a combination of a pure PDR contribution for o-H_2O 1_{10}-1_{01} (Poelman & Spaans 2005), and an embedded source for high excitation lines (Model I/II) in order to match the observations.

Table 3.7: Embedded Source Model

Transition	Wavelength	Average intensity model I	Average intensity model II	Average intensity PDR I (Sect. 3.3.2)
	[μm]	[erg cm^{-2}s^{-1}sr^{-1}]	[erg cm^{-2}s^{-1}sr^{-1}]	[erg cm^{-2}s^{-1}sr^{-1}]
o-H_2O 1_{10}-1_{01}	538.3	5.0×10^{-6}	2.2×10^{-6}	1.1×10^{-7}
o-H_2O 2_{12}-1_{01}	179.5	4.5×10^{-5}	1.4×10^{-5}	6.2×10^{-7}
o-H_2O 2_{21}-1_{10}	108.0	3.4×10^{-5}	1.4×10^{-4}	5.7×10^{-9}
o-H_2O 2_{21}-2_{12}	180.5	1.1×10^{-5}	3.8×10^{-5}	4.1×10^{-10}
o-H_2O 3_{03}-2_{12}	174.6	2.5×10^{-5}	5.4×10^{-5}	4.7×10^{-9}
o-H_2O 3_{12}-2_{21}	259.9	6.8×10^{-6}	3.1×10^{-5}	1.3×10^{-11}
o-H_2O 3_{12}-3_{03}	273.2	4.9×10^{-6}	1.6×10^{-5}	7.8×10^{-11}
o-H_2O 3_{21}-2_{12}	75.3	3.7×10^{-5}	2.2×10^{-4}	–
o-H_2O 3_{21}-3_{12}	257.7	2.7×10^{-6}	8.0×10^{-6}	–
o-H_2O 4_{14}-3_{03}	113.5	2.7×10^{-5}	1.3×10^{-4}	–
o-H_2O 3_{30}-3_{21}	136.5	5.0×10^{-6}	2.2×10^{-6}	–
p-H_2O 1_{11}-0_{00}	269.3	1.5×10^{-5}	1.5×10^{-5}	2.5×10^{-7}
p-H_2O 2_{02}-1_{11}	303.4	1.2×10^{-5}	1.0×10^{-5}	2.7×10^{-8}
p-H_2O 2_{20}-1_{11}	100.9	1.7×10^{-5}	1.4×10^{-4}	8.8×10^{-10}
p-H_2O 2_{11}-2_{02}	398.6	4.2×10^{-6}	4.6×10^{-6}	2.7×10^{-10}
p-H_2O 2_{20}-2_{11}	243.9	2.2×10^{-6}	1.4×10^{-5}	–
p-H_2O 3_{13}-2_{02}	138.5	1.8×10^{-5}	7.8×10^{-5}	–
p-H_2O 3_{13}-$2_{20}^{\dagger}$	1635.7	1.9×10^{-11}	1.6×10^{-7}	–
p-H_2O 3_{22}-2_{11}	89.9	1.8×10^{-5}	1.5×10^{-4}	–
p-H_2O 4_{04}-3_{13}	125.3	1.4×10^{-5}	9.5×10^{-5}	–

† Like Doty & Neufeld (1997) we find weak maser action in this line.

3.5 Line profiles

In this section, line profiles are presented for the 1_{10}-1_{01} transition of ortho-H_2O in the PDR, as well as the 3_{03}-2_{12} transition for a static embedded source.

In Figure 3.7, line profiles are plotted for a static PDR model (upper panels), and for a PDR with an outflow velocity field[1] (lower panels). A homogenous (*dotted*) and inhomogenous (*solid*) distribution have been considered. The left (*middle*) panel represents the line profiles when one takes the mean over a region, with a size comparable to the HIFI beam[2], toward

[1]The level populations, as calculated in Section 3.3.2 for the static PDR model are adopted because $\frac{dV}{dR}.L \sim \Delta v$.

[2]Half Power Beamwidth between 13″ and 39″, depending on frequency band.

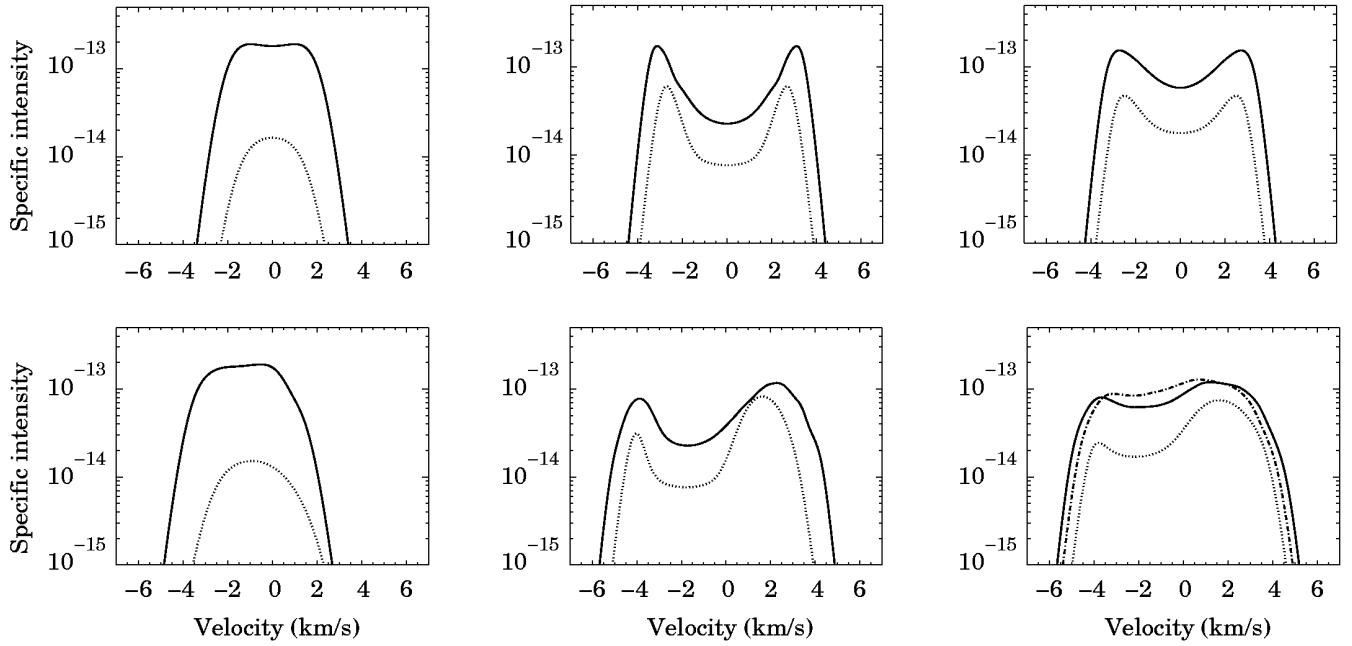

Figure 3.7: Line profiles for the 1_{10}-1_{01} transition in the case of a static PDR (*upper panel*) are plotted, where a systematic outflow velocity field is employed (*lower panel*). Line profiles are plotted when zooming in on a certain area in the PDR (left and middle plots), and when taking the mean over the PDR (right plots). The left (*middle*) plots represent the south-west (*north-east*) part of the cloud. Dotted (*solid*) lines are the line profiles in the case of an (*in*)homogeneous model. In addition, in the lower right panel a line profile for a model with a smaller clump size, $l_c = 0.02$ pc, is also plotted (*dash-dotted*). The Y-axis is in units of erg cm^{-2} s^{-1} sr^{-1} per cm s^{-1}.

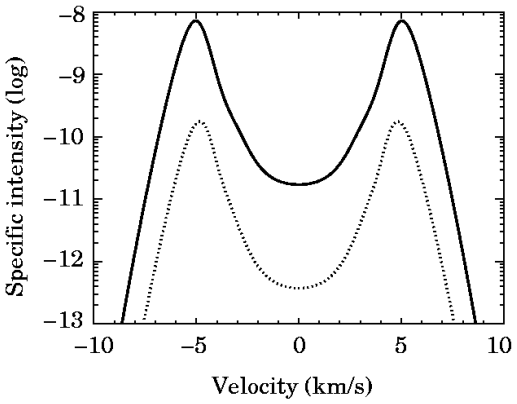

Figure 3.8: Line profiles for the 1_{10}-1_{01} (*dashed*) and 3_{03}-2_{12} (*solid*) transitions of o-H_2O for a static embedded source (*Model I*). The Y-axis is in units of erg cm^{-2} s^{-1} sr^{-1} per cm s^{-1}.

the south-west (*north-east*) side of the cloud. These two areas, L and R, are indicated by a circle in the upper left plot of Fig. 3.3. The upper and lower right plots depicts the line profiles when we take the mean over the PDR in its totallity.

Static line profiles

It is seen that different regions lead to different line shapes. This is due to the fact that at the western side of the cloud the abundance of water is lower, because of photodissociation, compared to the other side of the cloud. This leads to a lower water column, hence a lower opacity as opposed to the right side of the cloud. Consequently, a single-peaked line profile arises in the left part, whereas towards the right the line profile is self-absorbed due to opacity effects. In the inhomogeneous case, the clumps are the opacity source, increasing the opacity in the left part, resulting in a top-flatted profile. When taken the mean over the whole region, the line profiles are still self-absorbed. It is seen that the inhomogeneous distribution produces a higher intensity than the homogeneous distribution.

In Fig. 3.8 we plot line profiles for the o-H_2O 1_{10}-1_{01} and 3_{03}-2_{12} transitions arising from the static embedded source described in Section 3.4. One notices the difference with Fig. 3.7, in that the larger opacity in the lines causes the profiles to be very strongly self-absorbed. Inclusion of a velocity gradient with magnitude $\sim 3\,\Delta v_{\rm es}$ does not remove this self-absorption

characteristic.

Line profiles with a velocity field

Lower panels of Fig. 3.7 show line profiles for a PDR model with an outflow velocity field. We consider a velocity field, $V_{\rm out}$, ranging from -2 to $+2\,{\rm km\,s^{-1}}$, with a velocity equal to zero at the center, and gradually increasing towards the edge of the cloud, i.e., $V_{\rm out} \propto R$. A homogenous (*dotted*) and inhomogenous (*solid*) density distribution have been considered. The overall tendency of the shapes of the line profiles in the inhomogeneous case is comparable to the homogeneous models. In addition, a model with a smaller clump size $l_{\rm c} = 0.02\,{\rm pc}$ (dash-dotted), i.e., with clumps that are about 30% smaller is plotted. This clump size is consistent with other PDR characteristics (Spaans & van Dishoeck 1997) of S140.

We see that the line profile for the homogeneous model is more self-absorbed than when an inhomogeneous distribution is adopted. Reducing the clump size by a factor of 1.5, leads to a more single-peaked line profile, comparable with observations (Snell et al. 2000; Ashby et al. 2000). Although not shown, altering the velocity dispersion to $2\,{\rm km\,s^{-1}}$ broadens the line profile by a factor of ~ 2, in disagreement with observations.

If only microturbulence within the cloud is considered, stronger self-absorption effects occur than when macroturbulent motions are considered as well. The widths of the profiles are broader in the eastern part of the cloud, compared to the western side due to opacity effects. Note that the slopes of the line profiles depend on the adopted velocity dispersion. The differences between the slopes of the homogeneous and inhomogeneous models do not only depend on the density distribution (clumpiness versus homogeneity), but are also a result of the chemical and thermal balance within the clouds. Velocity fields with a moderate velocity gradient, as in $V_{\rm out}$, give rise to an almost top-flat line profile with a FWHM of $\sim 6\,{\rm km\,s^{-1}}$, in agreement with observations (Snell et al. 2000; Ashby et al. 2000). Similar results are found for an infall velocity field with a comparable velocity gradient.

3.6 Summary and discussion

In this chapter we have examined the influence of inhomogeneity on the excitation of water in molecular clouds. Inhomogeneity causes photons to penetrate much deeper into the cloud, leading to enhanced photodissociation of water. We have shown that intensities of PDR I and PDR II are a factor of a few higher as opposed to the intensities arising from a homogeneous distribution. PDR III is in closest agreement with the intensities of the homogeneous model. This is not surprising since the parameters of

PDR III resemble the homogeneous model most. We conclude that the major part of the water line intensity emanates from the warm high density clump edges.

The total antenna temperature, $T_A{}^*$, is reproduced for the o-H_2O 1_{10}-1_{01} line, observed by SWAS. However, the incorporated beam dilution factor is uncertain. It is found that the total signal is dominated by the signal of the PDR. Water line emission is found also outside of the PDR, but is a few orders of magnitude weaker, in agreement with observations (Snell et al. 2000). Freeze-out of water onto dust grains has not been taken into account. Bergin et al. (1995) probed the evolution of molecular clouds, including depletion of atoms and molecules onto grain surfaces in the temperature and density regime that we are interested in. They find that $50-60\%$ of the water vapour can be removed from the gas phase, when gas temperatures are $20-25$ K, dust temperatures 10 K and $\langle n_H \rangle = 10^3$ cm^{-3}, as in the case of the EMC. Consequently, depletion can result in an even lower intensity. We find for $n_H \sim 10^5$ cm^{-3}, $T_g = 25$ K and $T_d = 15$ K that $\sim 90\%$ of the water vapour is frozen-out (Bergin et al. 1995). However, depletion of water molecules in the PDR will occur only inside the shielded clumps (not the irradiated clump edges), and thus will not modify our results drastically.

Predictions have been made for the intensities and integrated antenna temperatures of various transitions that HIFI will probe in the future. It is found for S140 that the 2_{12}-1_{01} and 1_{11}-0_{00} transitions are the strongest for ortho- and para-H_2O, respectively, in all the models.

Ashby et al. (2000) present Monte Carlo radiative transfer models for the 557 GHz 1_{10}-1_{01} ground-state transition of ortho-H_2O in the S140 PDR observed by SWAS. These models adopt power-law representations for their density and temperature profiles, with the mean density of H_2 being a factor of ~ 40 larger than the density we adopted, $\langle n_{H_2} \rangle = 2 \times 10^4$ cm^{-3}, in our PDR models. They are unable to produce a single-peaked line profile with the observed integrated intensity by any combination of the ortho-H_2O abundance and turbulent velocity when a static cloud is adopted. A combination of turbulent and macroscopic motions, infall and/or outflow, is needed to reproduce the observed line profile. With our adopted density and temperature distributions, a single-peaked line profile is also not found for a static cloud. When an outflow (or infall) velocity field is incorporated, line profiles with a FWHM of ~ 6 km s^{-1} are obtained for a velocity field with a gradient of a few km s^{-1}. However, when modeling the line profiles for a static embedded source, with a size ~ 7 times smaller than the PDR, i.e., strongly beam-diluted in the SWAS $3.3' \times 4.5'$ beam, we find strongly self-absorbed line profiles that remain self-absorbed for modest velocity gradients.

On scales of the PDR, we see that the shapes of the line profiles in the inhomogeneous case are less self-absorbed than when an homogeneous model is adopted. At smaller scales, and comparable to the size of the HIFI beam,

different line profile shapes are found when zooming in on different areas of the PDR. Note that the beam of HIFI, depending on the frequency of the transition, will be ~ 5 times smaller than the PDR, being able to zoom in on certain regions, and to confirm the predicted change in the line profiles. Therefore, HIFI can distinguish the embedded sources from the PDR. The former produce a completely different emission line distribution (see Table 3.7), with the bulk of the emission emanating in lines like, e.g., 3_{21}-2_{21}, 3_{03}-2_{12}, 2_{12}-1_{01} and 2_{20}-1_{11}. Clearly, a combination of pure PDR and star-forming core characteristics is needed to plan for and interpret HIFI data.

Acknowledgements

We would like to thank Volker Ossenkopf for discussions on water observations with HIFI, and Wilfred Frieswijk for assistance with the figures. We would like to thank Matt Ashby for helpful discussions.

References

Ashby, M. L. N., Bergin, E. A., Plume, R., et al. 2000, ApJ, 539, L115
Ashby, M. L. N., Bergin, E. A., Plume, R., et al. 2000, ApJ, 539, L119
Bakes, E. L. O., & Tielens, A. G. G. M. 1994, ApJ, 427, 822
Beichman, C. A., Becklin, E. E., & Wynn-Williams, C. G. 1979, ApJ, 232, L47
Bergin, E. A., Langer, W. D., & Goldsmith, P. F. 1995, ApJ, 441, 222
Bergin, E. A., Neufeld, D. A., & Melnick, G. J. 1998, ApJ, 499, 777
Blair, G. N., Evans, N. J., vanden Bout, P. A., & Peters, W. L. 1978, ApJ, 219, 896
Boonman, A. M. S., Doty, S. D., van Dishoeck, E. F., et al. 2003, A&A, 406, 937
Cardelli, J. A., Mathis, J. S., Ebbets, D. C., & Savage, B. D. 1993, ApJ, 402, L17
Ceccarelli, C., Hollenbach, D. J., & Tielens, A. G. G. M. 1996, ApJ, 471, 400
Crampton, D., & Fisher, W. A. 1974, Spectroscopic observations of stars in HII regions Crampton and W. A. Fisher., Victoria: National Research Council of Canada, Radio and Electrical Engineering Division, Astrophysics Branch
Chen, W., & Neufeld, D. A. 1995, ApJ, 453, L99
Draine, B. T. 1978, ApJS, 36, 595
Draine, B. T., Roberge, W. G., & Dalgarno, A. 1983, ApJ, 264, 485
Elitzur, M., & de Jong, T. 1978, A&A, 67, 323
Elitzur, M., & Watson, W. D. 1978, A&A, 70, 443
Evans, N. J., Mundy, L. G., Kutner, M. L., & Depoy, D. L. 1989, ApJ, 346, 212
Falgarone, E., & Perault, M. 1988, A&A, 205, L1
Federman, S. R., Glassgold, A. E., Jenkins, E. B., & Shaya, E. J. 1980, ApJ, 242, 545
Graf, U. U., Genzel, R., Harris, A. I., et al. 1990, ApJ, 358, L49
Harvey, P. M., Campbell, M. F., & Hoffmann, W. F. 1978, ApJ, 219, 891
Helmich, F. P., van Dishoeck, E. F., Black, J. H., et al. 1996, A&A, 315, L173
Herpin, F., & Cernicharo, J. 2000, ApJ, 530, L129
Hayashi, M., Hasegawa, T., Gatley, I., Garden, R., & Kaifu, N. 1985, MNRAS, 215, 31
Hjalmarson, A., Frisk, U., Olberg, M., et al. 2003, A&A, 402, L39
Hogerheijde, M. R., van Dishoeck, E. F., Blake, G. A., & van Langevelde, H. J. 1998, ApJ, 502, 315

Keene, J., Blake, G. A., Phillips, T. G., Huggins, P. J., & Beichman, C. A. 1985, ApJ, 299, 967
Ladd, E. F., Fuller, G. A., & Deane, J. R. 1998, ApJ, 495, 871
Lee, J.-E., Bergin, E. A., & Evans, N. J. 2004, ApJ, 617, 360
Meixner, M., & Tielens, A. G. G. M. 1993, ApJ, 405, 216
Melnick, G. J., Stauffer, J. R., Ashby, M. L. N., et al. 2000, ApJ, 539, L77
Neufeld, D. A., Feuchtgruber, H., Harwit, M., & Melnick, G. J. 1999, ApJ, 517, L147
Neufeld, D. A., Lepp, S., & Melnick, G. J. 1995, ApJS, 100, 132
Neufeld, D. A., & Melnick, G. J. 1987, ApJ, 322, 266
Plume, R., Jaffe, D. T., & Keene, J. 1994, ApJ, 425, L49
Poelman, D. R., & Spaans, M. 2005, A&A, 440, 559
Preibisch, T., Balega, Y. Y., Schertl, D., Smith, M. D., & Weigelt, G. 2001, A&A, 378, 539
Preibisch, T., & Smith, M. D. 2002, A&A, 383, 540
Rawlings, J. M. C., & Yates, J. A. 2001, MNRAS, 326, 1423
Snell, R. L., Howe, J. E., Ashby, M. L. N., et al. 2000, ApJ, 539, L101
Spaans, M. 1996, A&A, 307, 271
Spaans, M., Tielens, A. G. G. M., van Dishoeck, E. F., & Bakes, E. L. O. 1994, ApJ, 437, 270
Spaans, M., & van Dishoeck, E. F. 1997, A&A, 323, 953
Spaans, M., & van Dishoeck, E. F. 2001, ApJ, 548, L217
Stark, R., Sandell, G., Beck, S. C., et al. 2004, ApJ, 608, 341
Stoerzer, H., Stutzki, J., & Sternberg, A. 1996, A&A, 310, 592
Stutzki, J., Stacey, G. J., Genzel, R., et al. 1988, ApJ, 332, 379
Truong-Bach, Sylvester, R. J., Barlow, M. J., et al. 1999, A&A, 345, 925
van der Tak, F. F. S., van Dishoeck, E. F., Evans, N. J., & Blake, G. A. 2000, ApJ, 537, 283
van der Tak, F. F. S., Boonman, A. M. S., Braakman, R., & van Dishoeck, E. F. 2003, A&A, 412, 133
van Dishoeck, E. F. 2004, ARA&A, 42, 119
van Dishoeck, E. F., Black, J. H., Boogert, A. C. A., et al. 1999, in ESA SP-427: The Universe as Seen by ISO, 437
Vejby-Christensen, L., Andersen, L. H., Heber, O., et al. 1997, ApJ, 483, 531
Williams, T. L., Adams, N. G., Babcock, L. M., Herd, C. R., & Geoghegan, M. 1996, MNRAS, 282, 413
Wright, C. M., van Dishoeck, E. F., Black, J. H., et al. 2000, A&A, 358, 689
Zhou, S., Butner, H. M., Evans, N. J., et al. 1994, ApJ, 428, 219